Volume 17, Issue 4, 172525 (1-15)

Iranian Journal of Earth Science (IJES)

https://doi.org/10.57647/j.ijes.2025.16847

Heat flow and thermal structural mapping of part of Middle Benue Trough for Exploration of Geothermal Energy

Oladiran Johnson Abimbola[1], Taiwo Adewumi[1,*], Hauwa Onyeka Iyima[1], Fidelis Iorzua Kwaghhua[2]

[1]*Department of Physics, Faculty of Science, Federal University of Lafia, Nigeria.*
[2]*Department of Geophysics, School of Physical Science, Federal University of Technology Minna.*

[*]**Corresponding author:** taiwo.adewumi@science.fulafia.edu.ng

Original Research

Received:
2024-05-31
Revised:
2024-09-26
Accepted:
2024-10-20
Published online:
2025-05-25
Published in issue:
2025-10-30

Abstract:

This study focuses on delineating the potency of geothermal energy within part of the Middle Benue Trough (MBT) via analyses of airborne geophysical datasets. The integrated analyses of airborne magnetic and radiometric data is to foster collaborative imaging and enhance the localization of target resources. A spectral analysis was performed on the total magnetic field of the study area to reveal the essential parameters that could be indicators of a potential geothermal reservoir. The analysis evaluated Curie point depth (CPD), geothermal gradient (GG), and heat flow (HF). Estimated values of CPD, GG, and HF range from 10 to 22.65 km, 25 to 55 °C/km, and 60 to 140 mW/m^2, respectively. Also, radiogenic heat production (RHP) range from 1.13 to 6.40 µW/m^3 was evaluated via analysis of airborne radiometric data. The RHP was estimated with respect to the lithologies in the study area. Sampling of element concentration and heat generation revealed that granitic rocks, schist, and shale hosted more radioelements and consequently contributed more to RHP within the study area. Viable HF and RHP for geothermal resources were observed at the mid-portion of the northern region, corresponding to Mada, Nasarawa Egon, Akwanga, and at the western and south-eastern edges, covering Udeni and Keana. The delineated major structures in NE-SW direction might serve as migration conduits and channels for crustal HF within the study area. The regions of high HF coincide with those of anomalous RHP, which might be attributable to the geological stability of the study area. This agreement is of priority and interest for geothermal exploitation in the study area.

Keywords: Geothermal energy; Heat flow; Curie point depth; Radiogenic heat production; Renewable energy

1. Introduction

Energy is a vital resource for national development. Over the years, insufficient power generation and distribution have retarded Nigeria's advancement as a developing country. The current generating sources, which are hydropower stations and gas-powered stations, have their shortfalls. Hydro-stations have low output during dry seasons due to a shortage of water; gas stations emit greenhouse gases, which are not ecosystem-friendly and are discouraged globally. Imperatively, industrialization, which is a core component of economic development, is powered by an adequate supply of electricity. This places the country in dire need of filling a huge energy deficit, and geothermal energy, when harnessed, will offer the desired alternative (Eletta and Udensi, 2012; Salako et al., 2020; Dimgba et al., 2020; Ekwok et al., 2021; Adewumi et al., 2021; Saadat et al., 2023; Adetona et al., 2023; Adewumi et al., 2024).

Geothermal energy is the heat produced in the internal layers of the earth, and studies have shown that two main sources contribute to the earth's internal heat, which are primordial heat and radiogenic heat. The Earth, though created more than 4.5 billion years ago, is continually cooling, thereby still retaining blaze of heat energy that birthed its formation and evolution in the form of primordial heat (Lay et al., 2008). The radioactive decay of materials in the mantle and crust of the Earth produces daughter isotopes,

releases geoneutrinos, and releases heat energy, also known as radiogenic heat. Three radioactive isotopes, uranium, thorium, and potassium, account for the majority of radiogenic heat due to their abundance in comparison to other radioactive isotopes (Korenaga, 2011; Šrámek et al., 2013; Schmeling et al., 2019).

Airborne magnetic data as a tool for studying the earth's subsurface relies on the magnetic susceptibility of rocks within the target regions. Over the years, studies have shown that aeromagnetic data is useful in identifying geologic structures such as faults, folds, shear zones, contacts, and intrusions, which are essential for localising magnetic minerals and delineating depth to geothermal reservoirs situated at the bottom of magnetic rocks (Paterson and Reeves, 1985; Airo, 2002; Ravat et al., 2007; Airo and Marit, 2010; Adewumi et al., 2019; Nazari et al., 2023). Numerous researches affirms the suitability of magnetic and radiometric data for mapping geothermal anomalies both on a regional and concise scale (Arjmandzadeh et al., 2017; Dimgba et al., 2020; Ekwok et al., 2021; Adewumi et al., 2021; Melouah et al., 2021; Abdelrahman et al., 2023; Alfaifi et al., 2023; Melouah et al., 2023; Adetona et al., 2024).

Suitable geophysical methods that could effectively and clearly image the subsurface and reveal the geothermal make-up of the study area are the pursuit of this study. The integration of both magnetic and radiometric methods will give a collaboratively useful result. Analysis of magnetic data will delineate geologic structures (fractures, faults, shear zones) that could be associated with geothermal reservoirs; compute the Curie point depth, geothermal gradient, and heat flow from aeromagnetic data analysis. Radiometric data analysis will estimate radiogenic heat production (RHP) from radioelements. Inferences from both analyses will be used to map prospective areas for geothermal energy exploration.

Several studies attempting to estimate the geothermal framework of the MBT and specifically Nasarawa State and environs were done, employing various conventional geophysical and geological prospecting methods. Borehole drilling, satellite imagery remote sensing, and airborne magnetic data analysis were applied at both regional and small-scale coverage (Bako, 2010; Anudu et al., 2012; Salako et al., 2020; Abdullahi and Kumar, 2020; Dopamu et al., 2021; Ngene et al., 2022; Alfaifi et al., 2023). However, the MBT region, and precisely Nasarawa and environs, has not been sufficiently subjected to the radiometric method of geothermal reservoir prospecting. Although the method has been successfully applied by several researchers around the world and in some parts of Nigeria for geothermal studies (Megwara et al., 2013; Ramadass et al., 2015; McCay et al., 2014; Kuforijimi and Christopher, 2017; Sanusi and Amigun, 2020; Adewumi et al., 2021; Adetona et al., 2023). It will be quite beneficial and impactful to implement the radiometric method of geothermal mapping within this current study due to its novelty in the region. The method is much more suitable for geothermal prospecting because, scientifically, it has been proven that a vast majority of the earth's heat is generated from the disintegration of radio elements (K, U, Th). Relatively, it can be inferred that an inspection of the abundance of these radioelements in the study region could also lead to the discovery of possible geothermal reservoirs (Adedapo et al., 2013; McCay et al., 2014). More precisely, this study aims to appropriately map the geothermal make-up of the study area via integration of magnetic and radiometric data sets. The estimation of radiogenic heat production (RHP), heat flow trends, and delineation of subsurface heat-conducting structural frameworks will further improve the reliability of the entire outcome of the study. Also, the lithology-based mode of RHP evaluation will be employed as a more detailed approach to capture the heat contribution of various lithologies within the study area. A combination of these study techniques will form a unique perspective of their application within the region of study. The results of this study will provide useful geophysical information on geothermal potential within part of Nasarawa State. This could serve as a guide for potential investors in the energy sector who could leverage the generated data to harness the underlying potent resources.

2. Location and geologic settings of the study area

The study area is part of North Central Nigeria located precisely in Nasarawa State. It is bounded by Longitude 8.0° E to 9.0° E and Latitude 8.0° N to 9.0° N (Fig. 1). The land cover is estimated to be 12, 100 km^2. The area cuts across major towns such as Akwanga, Lafia, Wamba and Doma. An express way which links the Federal Capital Territory to Benue state capital Markudi passes across the study area from Northern part at Akwanga to southern apart at Kardarko.

Geologically, the Middle Belt Trough (MBT) region is overlain by six Cretaceous formations including Asu River group, being the oldest, Ezeaku formation, Keana formation, Awe formation, Agwu formation and the Lafia formation

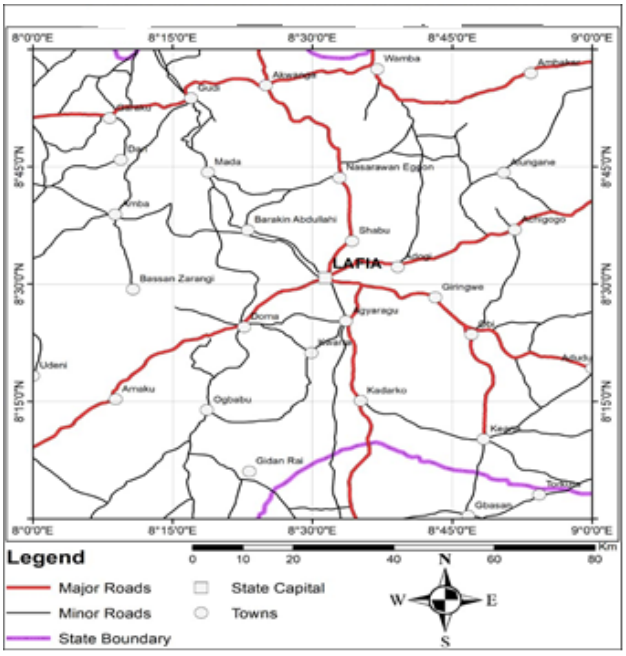

Figure 1. Location map of the study area (adapted from administrative map of Nigeria).

which is the most recent in the stratigraphic succession (Fig. 2). (Offodile, 1976; Nwajide, 1990). The Lafia formation which is also Maastrichtian, is part of the post-folding formation which terminated the sedimentation in the MBT. Within the study area, the sedimentary termination is seen as a demarcation along Nasarawa Eggon separating the sedimentary lithologies to the south and basement lithologies to the northern regions. The sediments are distinguished by sandstones, loose sands, flaky mudstones, alluvium, shale and limestones while the basement region is occupied by crystalline igneous intrusive such as porphyritic and biotite granite, migmatite, granite gneiss, undifferentiated schist and phylites, undifferentiated granite and migmatite (Obaje, 2009). The MBT was formed as a result of extensional tectonics during the breakup of the supercontinent Gondwana in the Cretaceous stage. The trough was subjected to multiple phases of rifting, subsidence, and inversion, leading to formation of various structural features, including faults, folds, and fractures.

3. Materials and methods

3.1 Data source

The airborne magnetic and radiometric datasets used for this study were obtained from the Nigeria Geological Survey Agency (NGSA). A digital format of the high resolution airborne geophysical datasets was part of the nationwide data collected and pre-processed by Fugro Airborne Surveys. The pre-processing involved removal of offset, diurnal and International Geomagnetic Reference Field (IGRF) for the magnetic data while background radiation interactions was filtered from the radiometric data. The survey parameters and specifications for both data sets is presented in Table 1.

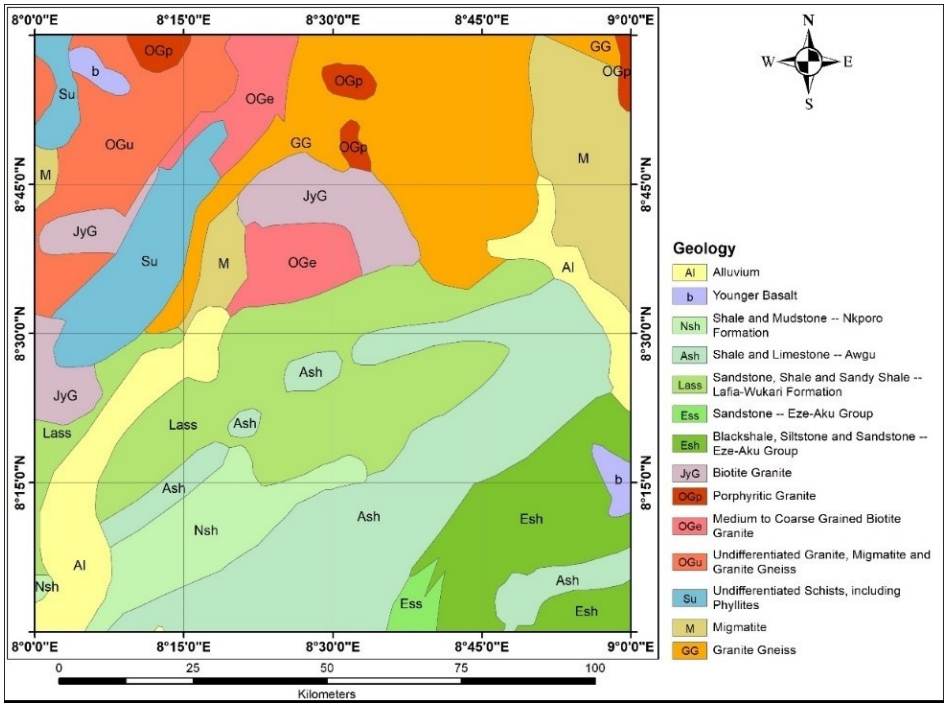

Figure 2. Geological map of the study area (NGSA, 2009).

Table 1. Data parameter and specifications (NGSA, 2009).

Survey Parameter	Magnetic Specifications	Radiometric Specifications
Data Acquired by:	Fugro Airborne Surveys	Fugro Airborne Surveys
Time Range	2005 – 2009	2005 – 2009
Data Recording Interval	0.1 seconds or less	0.1 seconds or less
Sensor Mean Terrain Clearance	80 meters	80 meters
Flight Line Spacing	500 meters	500 meters
Tie Line Spacing	5000 meters	2000 meters
Flight Line trend	135 degrees	135 degrees
Tie Line trend	45 degrees	45 degrees
Equipment: Aircraft	Cessna Caravan 208B ZS-FSA, Cessna Caravan 208 ZS-MSJ	Cessna Caravan 208B ZS-FSA, Cessna Caravan 208 ZS-MSJ
Equipment:	3 × Scintrex CS3 Cesium Vapour Magnetometer	(NaI "TI" crystals) 512-channels gamma-ray spectrometer

The area under investigation covers four (4) half-degree by half-degree (55 by 55 sq. km) data sheets of airborne magnetic and radiometric datasets which were knitted and used to produce the composite map of the total magnetic field (TMI) and the radioelement concentration maps (K, eTh, and eU) of the study area, respectively. All the datasets used for this study were filtered, enhanced, and processed using the Oasis Montaj^{TM}, Surfer, and MatLab software. The TMI gridded data were reduced to the magnetic equator to ensure proper placement of the magnetic anomalies over their causative bodies. Hence, the TMI reduced to equator (RTE-TMI) data were further analyzed to produce the vertical derivative (VD) maps, rose diagram (RD), analytic signal (ASG), and the geothermal parameter such as the CPD, geothermal gradient and heat flow. Also, the K, eTh, and eU were also utilised to generate the radiogenic heat production (RHP) maps. All the analysed maps were used to delineate the shallow-deep structural elements and thermal structures responsible for geothermal energy potential within the study area. The flowchart of the methods employed in this study for the geothermal-structural mapping is represented in (Fig. 3).

3.2 Geological structural mapping

3.2.1 Vertical derivative

The first vertical derivative is computed to help compress the deep sited magnetic source while enhancing the shallow and near surface features. For a study area located within the basement complex geology, the analysis will outline the geologic structural distortions, deformations and lineaments of magnetic sources. This will aid in amplifying the possibility of existing shallow Curie point depth underneath the near surface basement rock which is a pointer to potential geothermal reservoir occurrence. The first vertical derivative is computed from the formula:

$$L(r) = r^n \tag{1}$$

where n depict the order of differentiation generally 1 or 2, r signifies the wave number in radians per ground unit and L is cycle/ground unit in which the survey was conducted e.g. metres, feet, kilometre.

3.2.2 Analytic signal

The analytic signal analysis estimates the amplitude response of magnetic anomalies. The method simplifies the location of causative bodies in magnetic data by generating a bell-shaped symmetrical function for two-dimensional bodies and amplifying it for three-dimensional bodies, independent of factors like strike, dip, and magnetization (Debeglia and Corpel, 1997).

The analytic signal is a function related to magnetic fields by the derivatives:

$$\mathrm{AS} = \sqrt{\left(\frac{\partial A}{\partial X}\right)^2 + \left(\frac{\partial A}{\partial Y}\right)^2 + \left(\frac{\partial A}{\partial Z}\right)^2} \tag{2}$$

Interpretation of analytic signal maps and images provides simple indications of magnetic source geometry, with half

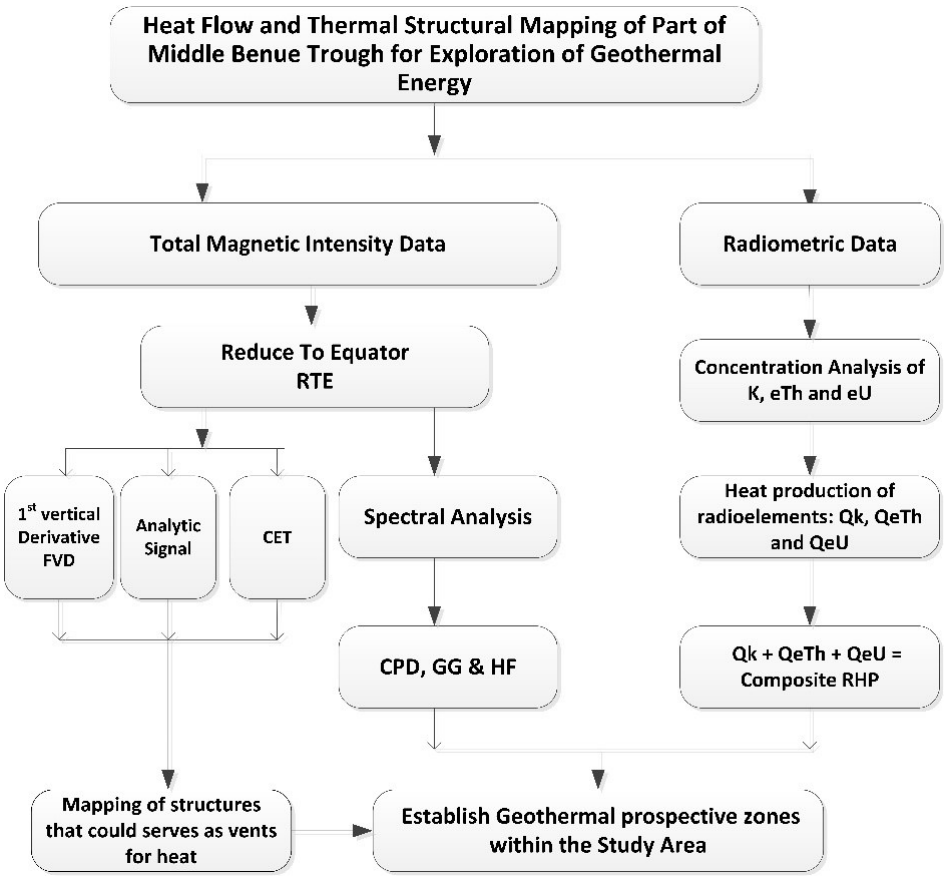

Figure 3. Flowchart of the methods employed for the geothermal-structural mapping.

widths linearly related to depths if sources are vertical magnetic contacts (Roest et al., 1992).

3.3 Thermal structural mapping and heat flow

3.3.1 Spectral depth analysis theory

The centroid method for evaluating depth to magnetic sources is reported as common and gives better depth estimates with less errors (Okubo et al., 1985; Ravat et al., 2007). The mathematical models of the centroid method are based on the examination of the shape of isolated magnetic anomalies introduced by Bhattacharyya and Leu (1975, 1977) and the study of the statistical properties of magnetic ensembles by Spector and Grant (1970). Blakely (1996) subsequently introduced power spectral density of total magnetic field, $\phi\Delta T(k_x,k_y)$as:

$$\phi\Delta T(k_x,k_y) = \phi_M(k_x,k_y)\cdot 4\pi^2 C_M^2 |\Theta_M|^2 |\Theta_f|^2 e^{-2|k|Z_t} \times (1-e^{-2|k|(Z_b-Z_t)})^2 \quad (3)$$

where k_x and k_y are wave numbers in x and y direction, $\phi_M(k_x,k_y)$ is the power spectra of the magnetization, C_M is a constant, Θ_M and Θ_f are factors for magnetization direction and geomagnetic field direction, and Z_b and Z_t are depths to bottom and top of magnetic layer respectively.
If the layer's magnetization, $M(x,y)$ is a random function of x,y it implies that $\phi_M(k_x,k_y)$ is a constant, and therefore the azimuthally averaged power spectrum, $\phi(|k|)$ would be given as:

$$\phi(|k|) = Ae^{-2|k|Z_t}(1-e^{-2|k|(Z_b-Z_t)})^2 \quad (4)$$

The depth to the top of the magnetic source is therefore derived from the slope of the high-wave-number portion of the power spectrum as:

$$\ln(P((k)^{\frac{1}{2}})) = A - |k|Z_t \quad (5)$$

where $P(k)$ is the azimuthally averaged power spectrum, k is the wave number (2π km^{-1}), A is a constant, and Z_t is the depth to the top of magnetic sources.
The centroid depth of magnetic sources can also be calculated from the low-wave-number portion of the wavenumber- scaled power spectrum as (Tanaka et al., 1999).

$$\ln(P((k)^{\frac{1}{2}}/k)) = B - |k|Z_0 \quad (6)$$

where B is a constant and Z_0 is the centroid depth of magnetic sources.
The depth to the bottom of the magnetic source (Z_b) can subsequently be obtained from the relation (Okubo et al., 1985).

$$Z_b = 2Z_0 - Z_t \quad (7)$$

Using the depth to the bottom of magnetic sources (Z_b), the geothermal gradient (dT/dZ)can be estimated as

$$\frac{dT}{dZ} = \frac{\Theta_c}{Z_b} \quad (8)$$

where Θ_c is the Curie temperature.
Next, using Z_b and dT/dZ, the heat flow (q_z) can similarly be estimated as (Okubo et al., 1985).

$$q_z = -\sigma\left(\frac{\Theta_c}{Z_b}\right) = -\sigma\left(\frac{dT}{dZ}\right) \quad (9)$$

where σ is thermal conductivity. Thermal conductivity of 2.5W/m/°C as the average for igneous rocks and a Curie temperature of 580°C (Stacey, 1977; Trifonova et al., 2009) are used as standard.

3.3.2 Radiogenic heat production (RHP)

The heat produced by radioactive decay in rock can be calculated using the equation developed by Rybach and Birch, for the energy released during radioactive decay (Rybach, 1976; Birch, 1954):

$$\mathrm{HP}(\mu\ \mathrm{W/m^3}) = \rho(0.0952\ \mathrm{C_U} + 0.0256\ \mathrm{C_{Th}} + 0.0348\ \mathrm{C_K}) \quad (10)$$

where: ρ is rock density (kg/m^3), $\mathrm{C_K}$ is concentration of potassium by % weight, $\mathrm{C_U}$ and $\mathrm{C_{Th}}$ are concentration of uranium and thorium in ppm. From equation (10), radioelement concentrations are multiplied by numerical constants, this reflects their differing contributions to radiogenic heat production in nW per kg of rock per unit of potassium, uranium or thorium. Uranium's constant is higher than potassium and thorium's, indicating its dominant role in heat production. To estimate the RHP of the study area, profile lines were drawn across each element concentration map to extract values of the radioelements. The extracted values were inputted into equation for calculating radiogenic heat production. The RHP was calculated with respect to the lithological units within the study area.

4. Results

4.1 Total magnetic intensity and reduce to equator maps

The trend of the magnetic signatures observed in the total magnetic intensity (TMI) and total magnetic intensity reduce-to-equator (TMI-RTE) maps recorded in nano tesla are represented in aggregate of colours over the study area (Fig. 4a and 4b). The spatially distributed values range from -41.4 to 113.8 nT and -35.9 to 111.2 nT, respectively. The TMI was reduced to magnetic equator using geomagnetic inclination and declination of –7.33° and 1.63°, respectively. The RTE filter enhances the position of the magnetic anomalies over their causative bodies. The northern regions are generally covered by high intensity values depicted in red to pink colours, which might be attributable to the dominant crystalline rocks. These include areas such as Akwanga, Mada, and Garaku in the northwestern regions, and Wamba, Nassrawa-Egon and Amboke on the northeastern regions. A sharp contrast of magnetic signatures is seen in the central and southwestern regions, corresponding to the Lafia and Udeni areas, respectively. These regions are depicted in deep blue colours signifying low magnetic intensities. The larger parts of southeastern regions with parts of south west are covered in yellow-red and green colours respectively signifying medium intensity values. The southern regions generally are covered by sedimentary rock formations that are low in magnetic susceptibility. Comparing the TMI-RTE to TMI, the RTE map (Fig. 4b) of the study

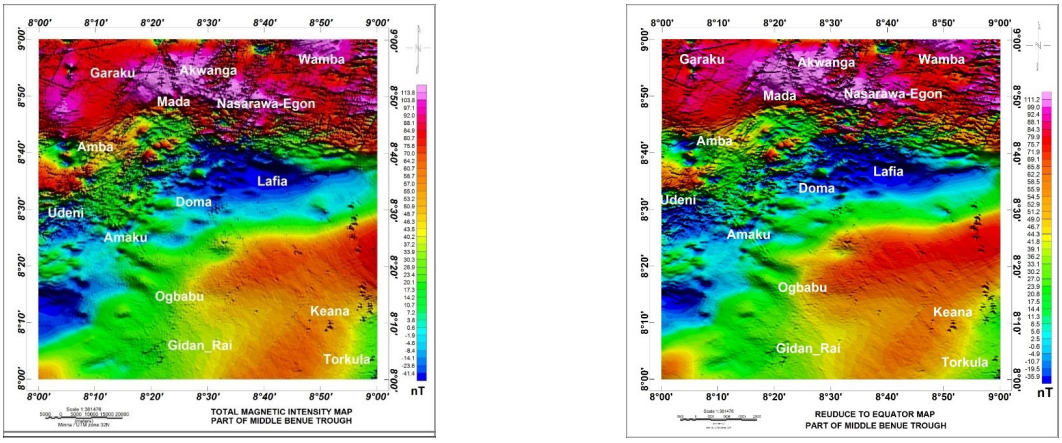

(a) **(b)**

Figure 4. (a) Total magnetic intensity map and (b) TMI reduce to magnetic equator map of the study area.

area reveals more aligned magnetic signatures over their causative bodies.

4.2 Delineation of structural trends

The first vertical derivative (FVD) map (Fig. 5a) is a measure of short- and long-wavelength anomaly trends. The short-wavelength anomalies at high frequencies are observed as distorted magnetic signatures occurring mainly in the northern half of the study area. They also signify shallow depth for magnetic sources, which are typical of basement terrains. The long-wavelength anomalies are observed in the southern half of the study area; they denote low magnetic intensities, which can be associated with sedimentary terrains. The blue lines on the first vertical derivative are the magnetic lineaments, while the yellow line indicates a lithological contact profile cutting across the study area in the middle region. The contact shows the termination of basement and sedimentary formations in the study area. The delineated lineaments in NE-SW, NW-SE direction on the first vertical derivative map can be associated with geologic structures such as fractures, folds, fault lines, and shear zones.

The analytic signal (AS) (Fig. 5b) is one of the analyses for delineating and enhancing geologic structures within the area of study. It is a measure of amplitudes computed to represent outcrops and shallow and deep-sited magnetic sources. The result clearly separates the northern regions of the study area, which are clustered by geologic structures, from the southern regions, which are devoid of near-surface structures. The northern regions mapped in red to pink colors can be associated with outcrops or shallow-sited magnetic sources with an amplitude range of 0.02 to 0.09. The near-surface features also signify basement complex terrane, while the low amplitudes ranging from 0.00 to 0.01 are regions of thick sedimentation and deeply sited magnetic sources. The regions of low amplitudes are observed from the middle regions towards the south and are more prominent at the south-eastern edge of the study area.

The lineaments map (Fig. 5c) shows the alignment of linear magnetic signatures, which can be associated with the geologic structural framework of the study area. Densely clustered lineaments are observed at the northern regions and the south-eastern edge. Both major and minor lineaments reflect structural deformations in basement rocks in the northern half and sedimentary formations in the southern regions of the study area. Geologic structures such as fractures, fault lines, folds, contacts, dykes, and shear zones are the results of various degrees of crustal deformation. Major lineaments are linked with elongated structures, while minor lineaments denote short distortions.

The rose diagram (RD) (Fig. 5d) is a representation of the directional trend of how structures are aligned within the study area. Major and minor structures are trending in the NE-SW, NNE-SSW, and E-W direction. The major structures delineated in Fig. 4a and 4b might serve as passage for the crustal heat, which might be utilised for geothermal energy in the study area.

4.3 Estimating the Curie point depth, geothermal gradient, and heat flow

For this study, sixteen (16) overlapping sub-sheets were mapped out and each subjected to Fast Fourier Transform (FFT) analysis. This process decomposes the magnetic data into its wave and energy spectral components. Both components were plotted using MATLAB with the log of energy on the vertical axis and the wavenumber component on the horizontal axis (Fig. 6). A straight line is fitted at the lower and higher wavenumber portions of the graph to generate gradients corresponding to the depth to the centroid (Z_0) and depth to the top (Z_t) of magnetic sources, respectively. The CPD is calculated from the values of depth to the centroid and top of magnetic sources using equation (7). The geothermal gradient is obtained when the Curie point depth is inputted into equation (8). Both CPD and geothermal gradient were used as inputs in equation (9) to evaluate the heat flow using a thermal coefficient of 2.5.

The geothermal parameters were obtained for each of the sixteen sub-sheets, and a coordinate corresponding to the centre of each sub-sheet was recorded (Table 2). Recorded coordinates for sixteen sub-sheets and values for each parameter were inputted into contouring software (Surfer Version 20). The resultant contour maps for Curie point depth,

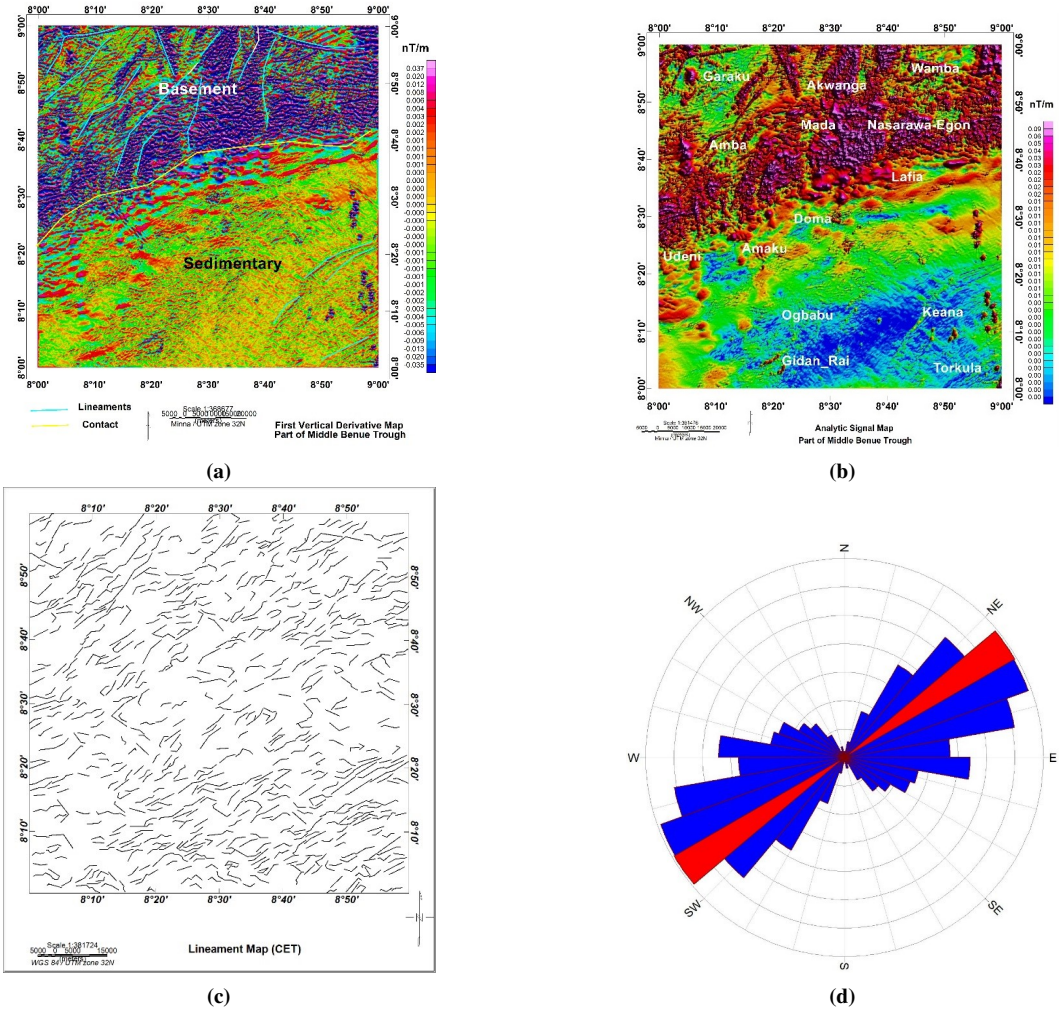

Figure 5. (a) Total magnetic intensity map and (b) TMI reduce to magnetic equator map of the study area.

geothermal gradient, and heat flow were generated to show the prevailing trend of each parameter across the study area. The CPD map of the study area (Fig. 7a) is a reflection of the depths to the bottom of magnetic sources mapped across the study area. The depth ranges indicate how far from the earth surface the Curie temperature of 580 °C can be reached. Estimated values ranged from 10 to 23 km, with an average of 16.30 km. The regions just above the central area, extending to the north-eastern regions, recorded deeper depths of 18 to 23 km. The deeper depths are mapped within the regions corresponding to Lafia, Shabu, and Aungane, depicted in blue to sky blue colors on the map. The north-west to south-western regions are mapped with a shallow depth range of 10 to 15 km. Areas such as Garaku, Amba, Bassan Zarangi, Udeni, Amaku, and part of Doma are mapped within the regions depicted in yellow, red, and purple colors on the map with a depth below 15 km.

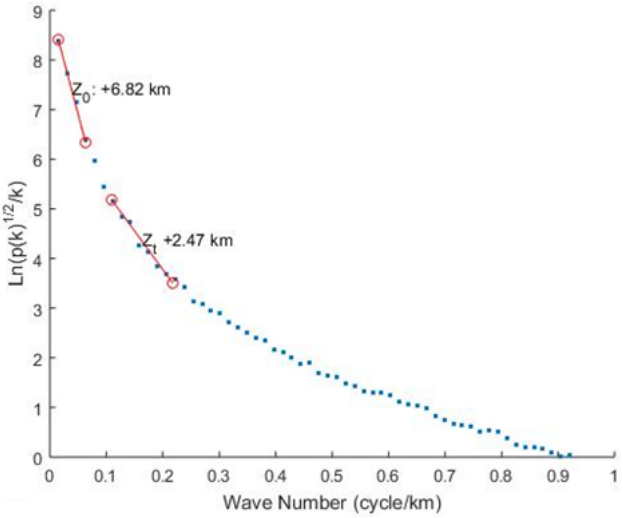

Figure 6. Spectral plot for block 1 indicating depth to top (Z_t) and centroid (Z_0).

The geothermal gradient (Fig. 7b) shows the variation of temperature with depth in kilometers; it's also a characteristic of the temperature gradients across the various regions of the study area. High values can be associated with potential geothermal reservoirs, while low values could denote a normal or no geothermal prospect. Within the study area, high temperature gradients are recorded along the northwest down to the southwestern regions. Estimated values ranging from 25 to 55°C/km were recorded, with an average of 37.40°C/km. The high ranges of 43 to 55°C/km are depicted in yellow to orange colors. North-eastern areas

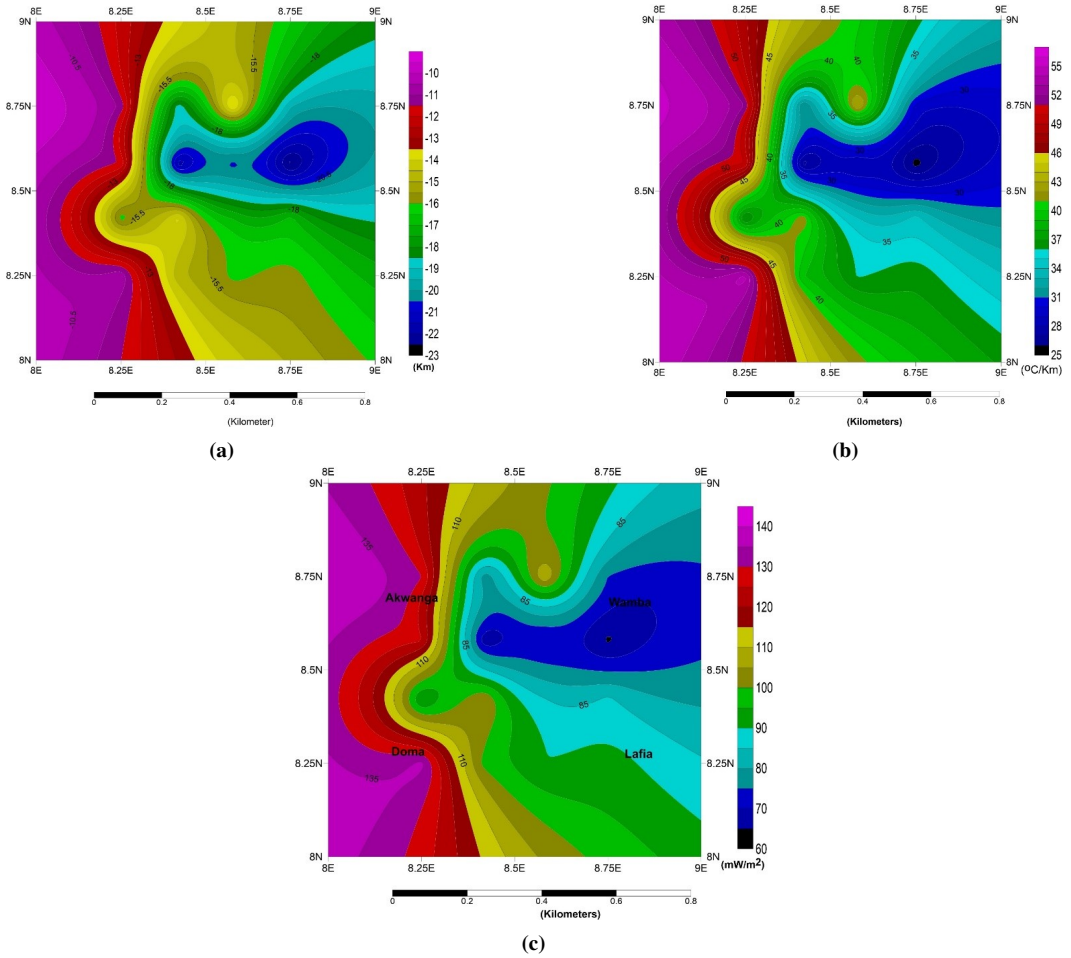

Figure 7. Contour map of; (a) CPD (b) geothermal gradient and (c) heat flow of the study area.

Table 2. Evaluated CPD, geothermal gradient, and heat flow of study area.

BLK	Lon	Lat	Depth to centroid Z_0 (km)	Depth to top Z_t (km)	Depth to bottom Z_b (km)	Geothermal gradient (°C/km)	Heat flow (mW/m^2)
1	8.25	8.75	6.82	2.47	11.17	51.92	130.32
2	8.42	8.75	10.5	2.23	18.77	30.90	77.56
3	8.58	8.75	8.34	3.34	13.34	43.48	109.13
4	8.75	8.75	10.5	1.56	19.45	29.82	74.85
5	8.25	8.58	6.51	1.42	11.60	50.00	125.5
6	8.42	8.58	12.5	3.20	21.80	26.61	66.79
7	8.58	8.58	12.0	3.40	20.60	28.16	70.68
8	8.75	8.58	12.0	1.35	22.65	25.61	64.28
9	8.25	8.42	10.3	4.36	16.24	35.71	89.63
10	8.42	8.42	8.06	2.23	13.89	41.76	104.8
11	8.58	8.42	9.90	2.76	17.04	34.03	85.44
12	8.75	8.42	9.83	2.78	16.88	34.36	86.24
13	8.25	8.25	7.04	3.41	10.67	54.36	136.44
14	8.42	8.25	8.80	2.77	14.83	39.11	98.17
15	8.58	8.25	9.61	3.08	16.14	35.94	90.21
16	8.75	8.25	9.92	4.04	15.80	36.71	92.14

such as Mada, Barakin Abdullahi, Adogi, Shabu, Lafia, and Achigogo are depicted in blue to purple, indicative of a low temperature gradient.

The heat flow map (Fig. 7c) reflects the geothermal makeup of the study area. Estimated values of 60 to 140 mW/m^2 were recorded, with an average of 93.88 mW/m^2. A range of heat flow above 80 mW/m^2 is considered high and meets an exploitable threshold. The entire study area shows prevailing heat flow values above 80 mW/m^2, with the exception of areas around Wamba in the central to north-eastern region. The northwest, down to the southwestern regions, recorded peak values from 110 to 140 mW/m^2 within areas such as Garaku, Dari, Amba, Bassan Zarangi, Udeni, Amaku, Ogbabu, and Gidanrai. The south-eastern regions recorded values between 85 and 110 mW/m^2.

4.4 Radioelements concentration maps of the study area

The concentration of radiogenic elements (K, eTh, and eU) was estimated within the study area in percentage for K and parts per million (ppm) for eTh and eU. The average values of each element were measured from different lithology units within the study, as allotted by the geology map in Fig. 2. The extracted values helped define the spatial spread of the elements relative abundance across the study area (Figs. 8a, 8b, and 8c). Regions of high concentrations (HC) are depicted in red to pink colours, while regions of medium to low concentrations (LC) are depicted in green to blue colours. The map for potassium (Fig. 8a) shows that high concentrations occurred mainly in the northern regions. A sharp contrast to low concentrations is observed in the central regions corresponding to Lafia, Doma, and Agyaragu. The south-west also shows significant low concentrations in regions around Amaku and Gidan Rai. Medium concentrations are observed at the south-eastern edge. Majorly high concentrations occurred within the crystalline basement formations, while low concentrations were recorded in the sedimentary lithological formations. The equivalent thorium concentration map (Fig. 8b) shows peak concentrations at the central-north, western, and south-eastern edges, corresponding to Mada-Nassarawa Egon, Udeni, and Torkura areas, respectively. An isolated area of low concentration around Gidan Rai in the south west is surrounded by medium concentrations expanded from the center to the south east and part of the south west. A remarkably large area of low concentration is observed from Doma to Amaku on the western flank of the study area. The concentration of equivalent uranium (Fig. 8c) followed a similar trend to that of thorium. Notable high concentrations were observed at the north, western, and south-eastern edges. An isolated low concentration is observed, surrounded by medium con-

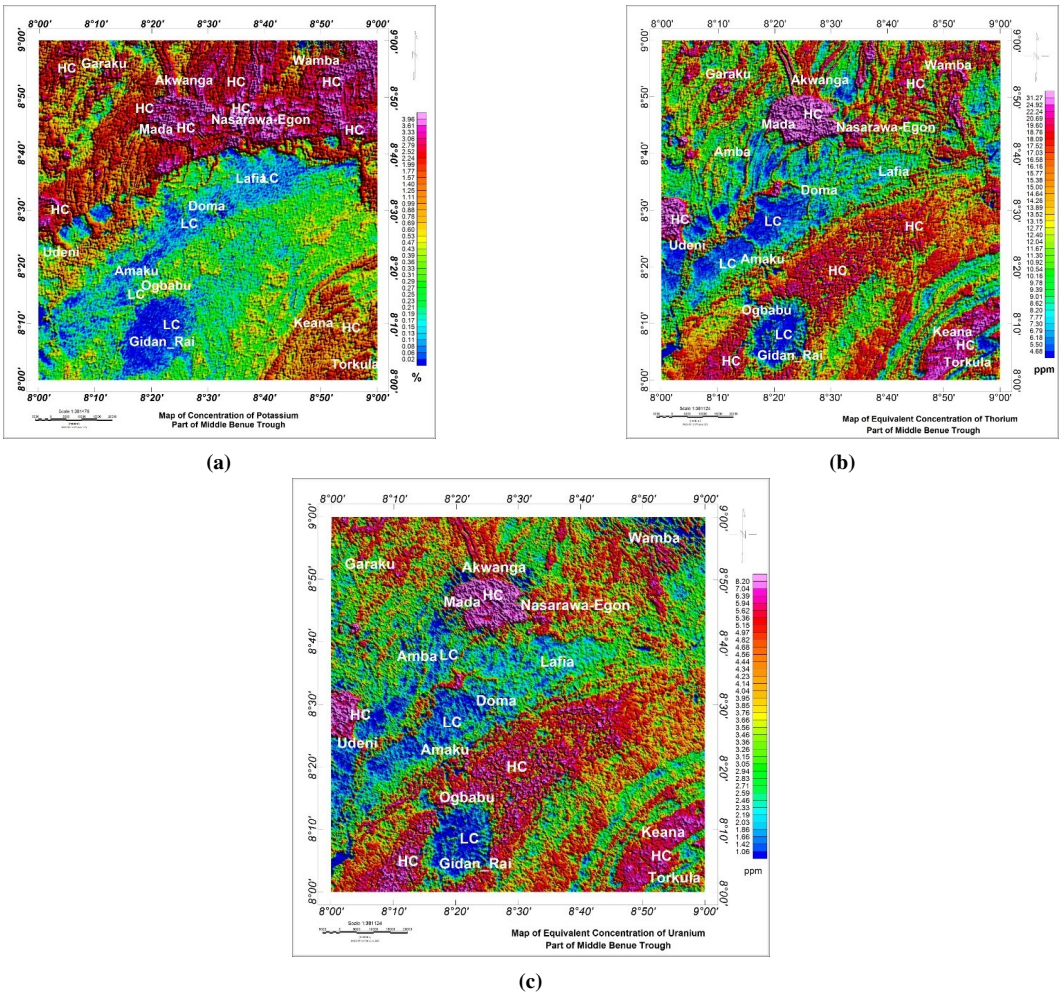

(a) **(b)** **(c)**

Figure 8. Concentration map of; (a) Potassium K (b) Thorium eTh and (c) Uranium eU of the study area.

centrations in the southwestern region. A similar but large concentration also occurred at the western flank, covering areas such as Doma, Amaku, and Udeni.

4.5 Radiogenic heat production (RHP) of the study area

The RHP for each of the radioelements and the total RHP were produced using equation (10). The summary of the calculated RHPs with their respective lithologies are presented in Table 2 showing the contribution of the rocks to heat generation within the study area. The heat production due to potassium (Fig. 9a) ranges from 0.05 to 0.75 μW/m^3. The basement half of the study area within the northern regions recorded high values from 0.15 to 0.75 μW/m^3 while the sedimentary southern region extending from the center recorded values of 0.1 μW/m^3 and lower. Potassium's peak heat values were contributed by granitic rock unite situated in the extreme north-west and north-eastern regions of the study area. Likewise, the RHP due to equivalent thorium (Fig. 9b) ranges from 0.3 to 2.3 μW/m^3, with an average of 0.8 μW/m^3. High values at the mid portion and eastern edge of the northern regions are related to presence of porphyritic granite, schist, and migmatite. Areas corresponding to Wamba, Akwanga, and northern environs recorded peak heat productions ranging from 0.9 to 2.3 μW/m^3. The southern half from the center recorded values from 0.8 μW/m^3 and lower with exception of south-eastern edge. Also, the RHP due to equivalent Uranium (Fig. 9c) exceeded that of potassium and equivalent Thorium. Values ranging from 0.4 to 3.65 μW/m^3 were recorded across study area. RHP values between 1 to 3 μW/m^3 were mainly due to presence of eU in shale, schist and granite.

5. Discussion

5.1 Delineation of structural trends

Geological structures such as faults and lineaments play a significant role in geothermal prospecting. They serve as a vent/conduit for the migration of heat generated and stored in the geothermal reservoir to its manifestation on the earth's surface. The structural trends within the study area were effectively delineated using FVD, AS, RD, and lineament map generated from centre for exploration targeting (CET) (Fig. 5a-5d). Both minor and major structures were delineated with major structures oriented in NE-SW, NNE-SSW, and NW-SE directions. The dominant structural trending can be inferred from the RD and lineament maps (Fig. 5c-5d). These structures can be associated with geologic structures such as faults, fractures, folds, and shear zones. The occurrence of these structures can be linked with possible vents and conduit channels through which geothermal energies reaches the earth surface from the geothermal reservoir.

5.2 Mapping the heat flow and thermal structures: Insight from magnetic and radiometric analyses

For proper evaluation of geothermal anomalous zones, which might result from volcanic eruptions, igneous intrusions, and tectonic activities in the study area, the spectral magnetic depth analytical method is employed to determine the CPD, geothermal gradient, and heat flow. Also, the radioelement concentrations are used to estimate the RHP, which might occur from the decay of the naturally occurring radioisotopes. The radiogenic heat production from each radioelement was computed from their rock units of composition in varying proportions across the study area. The trend of occurrence of the three elements is observed differently both in the northern basement half and southern sedimentary regions. The individual contribution to heat production by elements also varied according to their relative abundance and intensity of radioactivity. The total RHP map of the three radioelements integrated with the lineament map gives the composite RHP map in Fig. 9d. The values of RHP were computed from the composition and relative abundance of the radioelements within the lithology units of the study area. Consequently, this was reflected in the amount of heat contributions by different rock units within the study area. RHP varies measurably and significantly with lithologies due to variations in concentrations of K, eTh, and eU (Haack, 1982; Čermák and Rybach, 1982). The estimation of RHP in sedimentary rocks varies considerably compared to crystalline basement rocks. A comparative sampling revealed granitic rocks and undifferentiated schist within the basement half, with shale in the sedimentary regions as the top contributors to the RHP (Table 3). Porphyritic granite values range from 2.10 to 6.4 μW/m^3, biotite granite and undifferentiated Schist recorded 1.29 to 4.7 μW/m^3, gneiss granite and migmatite gave a range of 2.18 to 4.78 μW/m^3, shale, limestone, and sandstone values range from 1.911 to 3.40 μW/m^3, and alluvium sediments contributed the least RHP in the range of 1.13 to 1.77 μW/m^3 (Table 3). The lineaments mapped within the regions of high RHP serve as evidence of channels for heat migration in the subsurface that can be harnessed. Superimposed on the total RHP map (Fig. 9d) are the lineaments. The delineated structures (faults) on the geothermal zones observed in Fig. 9d trend predominantly in the NE-SW direction, which might serve as a migratory path or trap for the crustal heat in the study area.

5.3 Viable areas within the study for geothermal resources

The results of the spectral analysis indicate high geothermal parameters in all regions, with the exception of areas around Lafia extending to the eastern edge of the study area. This implies that all other regions recorded values of 80 mW/m^2 and above, which is favourable for good geothermal sources (Cull and Conley, 1983; Jessop, 1976). These range of result values also aligns with outcomes of previous regional studies across the globe (Akinyemi and Zui, 2019; Abdullahi et al., 2023; Dopamu et al., 2021; Salako et al., 2020; Dimgba et al., 2020; Adewumi et al., 2021; Adewumi et al., 2024). The trend of estimated heat flow also compares favourably with results obtained via satellite imagery and regional gravity data analysis within the Middle Benue Trough (Ngene et al., 2022).

Radiometric analysis estimated RHP values largely above the limit of 2.5 μW/m^3 as the crustal average. Anomalous RHP values exceeding the conventional crustal average were recorded. A range of 4.0 to 6.4 μW/m^3 was estimated

Table 3. Summary of the radiogenic heat production with their respective lithologies and coordinate.

S/N	X	Y	Rock ID	Rock Type	K (%)	eTh (ppm)	eU (ppm)	Qk (μW/m^3)	QeTh (μW/m^3)	QeU (μW/m^3)	RHP (μW/m^3)
1	8.5489	8.746	GG1	Granite Gneiss	2.4	16.6	12.6	0.23	1.18	3.35	4.78
2	8.6587	8.9423	GG2		2.3	16.1	6.7	0.22	1.15	1.78	3.16
3	8.7	8.7356	GG3		2.7	12.7	6.1	0.26	0.91	1.62	2.79
4	8.6787	8.8649	GG4		2.7	14.5	5.5	0.26	1.04	1.46	2.76
5	8.7275	8.7684	GG5		1.7	14.3	7.5	0.16	1.03	1.99	3.19
6	8.8657	8.8347	M1	Migmatite	3.5	22.8	9.3	0.34	1.63	2.47	4.45
7	8.9153	8.7533	M2		2.3	14.0	8.0	0.22	1.01	2.13	3.36
8	8.9733	8.7535	M3		2.3	9.2	6.2	0.22	0.65	1.65	2.53
9	8.2965	8.5859	M4		1.0	7.9	5.7	0.09	0.56	1.52	2.18
10	8.4319	8.607	OGE1	Medium to	0.7	8.0	3.1	0.06	0.54	0.77	1.38
11	8.4274	8.5799	OGE2	Coarse	0.5	11.0	6.3	0.05	0.74	1.58	2.37
12	8.4284	8.5458	OGE3	Biotite	0.2	7.8	4.0	0.02	0.52	1.01	1.55
13	8.3431	8.8558	OGE4	Granite	1.8	12.4	7.4	0.16	0.83	1.85	2.86
14	8.3513	8.9011	OGE5		1.2	18.4	14.9	0.11	1.24	3.74	5.09
15	8.0574	8.7557	OGU1	Undifferentiated	0.9	11.2	5.2	0.08	0.75	1.31	2.15
16	8.0893	8.7513	OGU2	Granite	0.9	12.7	6.8	0.08	0.85	1.71	2.65
17	8.1589	8.7864	OGU3		0.9	15.1	6.6	0.08	1.02	1.65	2.76
18	8.1544	8.8089	OGU4		1.4	14.4	10.2	0.12	0.97	2.56	3.66
19	8.1373	8.8887	OGU5		1.3	16.8	6.9	0.12	1.13	1.73	2.98
20	8.4899	8.7164	JYG1	Biotite Granite	2.5	23.1	11.7	0.22	1.56	2.94	4.73
21	8.4864	8.6847	JYG2		2.1	15.5	13.4	0.19	1.05	3.36	4.61
22	8.4814	8.6482	JYG3		1.4	9.4	4.6	0.13	0.64	1.15	1.92
23	8.5183	8.666	JYG4		1.5	14.3	11.4	0.14	0.96	2.86	3.96
24	8.017	8.3652	JYG5		0.4	5.9	3.4	0.04	0.39	0.85	1.29
25	8.1322	8.603	SU1	Undifferentiated	1.9	16.2	12.5	0.17	1.09	3.14	4.41
26	8.1383	8.5714	SU2	Schist	1.4	13.6	9.0	0.12	0.92	2.26	3.31
27	8.1926	8.5811	SU3		1.4	8.3	3.8	0.13	0.56	0.95	1.64
28	8.018	8.871	SU4		1.6	11.9	4.6	0.14	0.80	1.15	2.11
29	8.1869	8.9558	OGP1	Porphyritic	1.0	12.5	6.1	0.95	0.87	1.59	3.42
30	8.1809	8.9511	OGP2	Granite	1.1	11.2	5.2	0.11	0.78	1.35	2.24
31	8.1966	8.9442	OGP3		0.7	11.5	5.7	0.06	0.81	1.49	2.36
32	8.5144	8.8787	OGP4		2.8	10.2	8.0	0.26	0.72	2.09	3.06
33	8.5027	8.7624	OGP5		3.2	32.6	14.6	0.31	2.28	3.81	6.40
34	8.991	8.924	OGP6		4.0	13.1	8.4	0.38	0.92	2.19	3.49
35	8.167	8.2688	LASS1	Shale	0.2	10.7	7.0	0.02	0.65	1.59	2.27
36	8.2531	8.3303	LASS2		0.2	10.6	7.8	0.02	0.65	1.78	2.45
37	8.3947	8.407	LASS3		0.1	11.9	8.4	0.01	0.73	1.91	2.65
38	8.6636	8.5308	LASS4		0.2	12.2	7.4	0.02	0.74	1.69	2.45
39	8.488	8.3271	LASS5		0.3	18.6	9.5	0.02	1.14	2.17	3.33
40	8.5042	8.3718	LASS6		0.2	16.8	10.3	0.02	1.03	2.35	3.40
41	8.887	8.4335	ASH1	Limestone	0.4	14.5	5.8	0.04	0.94	1.41	2.39
42	8.7251	8.3236	ASH2		0.4	12.8	6.8	0.04	0.83	1.65	2.52
43	8.763	8.2696	ASH3		0.4	16.3	2.4	0.03	1.06	0.58	1.68
44	8.5956	8.1991	ASH4		0.3	13	8.3	0.03	0.84	2.01	2.89
45	8.6131	8.1519	ASH5		0.3	12.4	5.7	0.03	0.81	1.38	2.22
46	8.199	8.1844	ASH6		0.1	12.1	5.7	0.01	0.78	1.38	2.18
47	8.2309	8.1503	NSH1	Shale and	0.2	15.3	10.7	0.02	0.94	2.44	3.40
48	8.2146	8.0821	NSH2	Mudstone	0.2	14.4	10.7	0.02	0.88	2.44	3.34
49	8.2982	8.1104	NSH3		0.1	10.8	8.6	0.01	0.66	1.96	2.63
50	8.9081	8.5453	AL1	Alluvium	0.3	13.9	5.5	0.02	0.71	1.04	1.77
51	8.1577	8.3326	AL2		0.4	6.8	4.0	0.03	0.34	0.76	1.13
52	8.0529	8.1651	AL3		0.2	9.7	4.6	0.01	0.49	0.87	1.38
53	8.8115	8.2098	ESH1	Sandstone	0.9	11.3	5.0	0.07	0.69	1.14	1.91
54	8.8505	8.1675	ESH2		1.1	15.2	6.4	0.09	0.93	1.46	2.48
55	8.9117	8.117	ESH3		0.9	15.8	6.5	0.07	0.97	1.48	2.53
56	8.8529	8.0394	ESH4		1.3	16.4	7.3	0.11	1.01	1.66	2.78

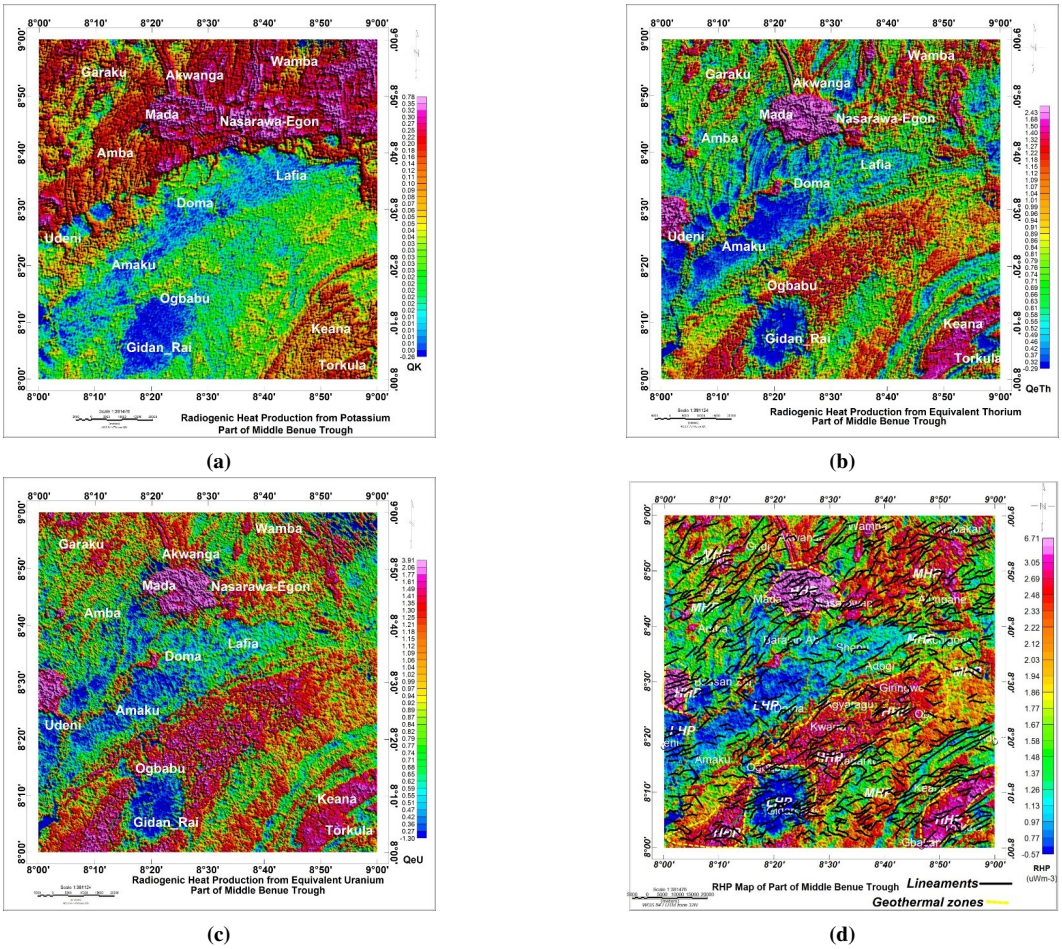

Figure 9. Radiogenic heat production from; (a) K concentration (b) eTh concentration (c) eU concentration and (d) total RHP of the study area.

in some regions and is indicative of a viable geothermal occurrence (McCay et al., 2014; Bakar et al., 2023).

The regions of interest for mapping geothermal zones will be areas with positive geothermal parameters from both spectral analysis of magnetic data and statistical sampling of radiogenic elements. Correlating the two analyses, it can be deduced that regions of high heat flow within 85 to 110 mW/m^2 also recorded anomalous RHP in the range of 4.0 to 6.4 µW/m^3, which might be attributable to geological stability, similar lithology, thermal conductivity, and geothermal gradient of the study area. These ranges of values from both analyses meet recommended estimates for a viable geothermal source. Hence, the areas of Mada, Nasarawa-Egon and Akwanga at the mid portion of northern region, Udeni at western edge with Ogbabu, Keana and Torkula at south eastern region, are areas noted to have features that favour geothermal exploration within the study area.

6. Conclusion

The integrated analysis of airborne magnetic and radiometric data within part of the middle Benue trough revealed a clearer image of subsurface geothermal compositions within the study area. The results of the spectral depth analysis performed on the airborne magnetic data evaluated the essential parameters that were indicative of a good geothermal prospect. Geologic features, including fault lines, shear zones, folds, and fractures, can be linked to the defined lineaments on the first vertical derivative map. The presence of these formations in the study area may be connected to potential vents and conduit channels that allow geothermal energy to reach the earth's surface. Sufficient research shows that shallow Curie point depth, a high geothermal gradient, and heat flow favor the siting of a good geothermal source. Shallow CPD and anomalous heat flow of 110 to 140 mW/m^2 were recorded in the western regions (NW and SW), indicating a highly resourceful geothermal region. Other regions of the study area, with the exception of the central regions extending to the eastern edge, recorded heat flow values of 85 to 110 mW/m^2. These ranges of values fall within the conventional threshold of a good geothermal source and denote a wide coverage of ripped geothermal zones across the study area.

Results of the radiometric analysis shows rock units harbouring radioactive elements within the study area that maintain a high geothermal gradient in the regions. A lithology-based evaluation of radioelements and their heat generation capacity revealed that granitic variants (biotite, porphyritic, gneiss, grained, and coarse), schist, and shale were major contributors to the RHP of the study area. The recorded radiogenic heat production due to continuous disintegration of the radiogenic elements exceeds the conventional average of 4.0 µW/m^3 for a potential geothermal source. Anomalous RHP of 4.0

to 6.4 μW/m^3 was observed in the mid-portion of the northern region, the western edge, and the south-eastern region. Also, the lineament map superimposed on the RHP map clearly shows evidence of structures that serve as channels for heat migration in the subsurface. Both results collaboratively map zones of prospective viable geothermal sources. Regions of high heat flow coinciding with anomalous RHP are of interest and are mapped as geothermal prospective zones. These areas are: Mada, Nasarawa-Egon, and Akwanga in the mid-northern regions; Udeni at the western edge; and Ogbabu, Keana, and Torkula in the south-eastern region.

A direct geophysical method such as the magnetotelluric method can further be used in the delineated geothermal anomalous zones for geothermal resource exploitation in the study area. The harnessed geothermal energy will be used to complement the existing energy base of the study area and its environs.

Funding Statement

This research was supported by a 2024 Institutional Based Research (IBR) grant from the Tertiary Education Trust Fund (TETFund) of Nigeria.

Authors contributions

Authors have contributed equally in preparing and writing the manuscript.

Availability of data and materials

The data that support the findings of this study are available from the corresponding author, upon reasonable request.

Conflict of interests

The authors declare that they have no known competing financial interests or personal relationships that could have appeared to influence the work reported in this paper.

References

Abdelrahman K., Ekwok S. E., Ulem C. A., Eldosouky A. M., Al-Otaibi N., Hazaea B. Y., Akpan A. E. (2023) Exploratory mapping of the geothermal anomalies in the Neoproterozoic Arabian Shield, Saudi Arabia, using magnetic data. *Minerals* 13 (5): 694. DOI: https://doi.org/10.3390/min13050694.

Abdullahi M., Kumar R. (2020) Curie depth estimated from high-resolution aeromagnetic data of parts of lower and middle Benue trough (Nigeria). *Acta Geodaetica et Geophysica* 55 (4): 627–643. DOI: https://doi.org/10.1007/s40328-020-00314-4.

Abdullahi M., Valdon Y. B., Andrew F. P., Idi B. Y. (2023) Curie Depth and Surface Heat Flow Estimation from Anomalous Magnetic Blocks in the Lower and Part of Middle Benue Trough and Anambra Basin. *Earth and Planetary Science* 2 (1): 11–20. DOI: https://doi.org/10.36956/eps.v2i1.821.

Adedapo J. O., Kurowska E., Schoeneich K., Ikpokonte A. (2013) Geothermal gradient of the Niger Delta from recent studies. *International Journal of Scientific and Engineering Research* 4 (11): 1–5.

Adetona A. A., Fidelis I. K., Shakarit B. A. (2023) Interpreting the magnetic signatures and radiometric indicators within Kogi State, Nigeria for economic resources. *Geosystems and Geoenvironment* 2 (2): 100157. DOI: https://doi.org/10.1016/j.geogeo.2022.100157.

Adetona A. A., Rafiu A. A., Aliyu B. S., John M. K., Kwaghhua I. F. (2024) Estimating the Heat Flow, Geothermal Gradient and Radiogenic Heat within the Young Granites of Jos Plateau North Central Nigeria. *Journal of the Earth and Space Physics* 49 (4)

Adewumi T., Abimbola O., Madaki A. U., Kwaghhua F. I., Lawal S. M. (2024) Mapping of subsurface thermal structures of Gongola Basin, NE Nigeria from airborne magnetic and gamma-ray spectrometry data: implication for geothermal prospecting. *Journal of the Earth and Space Physics,* DOI: https://doi.org/10.22059/jesphys.2024.361511.1007537.

Adewumi T., Salako K. A., Adediran O. S., Okwoko O. I., Sanusi Y. A. (2019) Curie point Depth and Heat Flow Analyses over Part of Bida Basin, North Central Nigeria using Aeromagnetic Data. *Journal of Earth Energy Engineering* 8 (1): 1–11. DOI: https://doi.org/10.25299/jeee.2019.vol8(1).2288.

Adewumi T., Salako K. A., Usman A. D., Udensi E. E. (2021) Heat flow analyses over Bornu Basin and its environs, Northeast Nigeria, using airborne magnetic and radiometric data: implication for geothermal energy prospecting. *Arabian Journal of Geosciences* 14 (4): 1–19. DOI: https://doi.org/10.1007/s12517-021-07370-2.

Airo M. (2002) Aeromagnetic and Aeroradiometric Response to Hydrothermal Alteration. *Surveys in Geophysics* 23 (5): 273–302. DOI: https://doi.org/10.1023/A:1015556614694.

Airo M., Marit W. (2010) Application of regional aeromagnetic data in targeting detailed fracture zones. *Journal of Applied Geophysics* 71 (3): 62–70. DOI: https://doi.org/10.1016/j.jappgeo.2010.03.003.

Akinyemi L., Zui V. I. (2019) Summary of heat flow studies in Nigeria. *Journal of the Belarusian State University. Geography and Geology* 2:121–132. DOI: https://doi.org/10.33581/2521-6740-2019-2-121-132.

Alfaifi H. J., Ekwok S. E., Ulem C. A., Eldosouky A. M., Qaysi S., András P., Akpan A. E. (2023) Exploratory assessment of geothermal resources in some parts of the Middle Benue Trough of Nigeria using airborne potential field data. *Journal of King Saud University-Science* 35 (2): 102521. DOI: https://doi.org/10.1016/j.jksus.2022.102521.

Anudu G. K., Onuba L. N., Onwuemesi A. G., Ikpokonte A. E. (2012) Analysis of aeromagnetic data over Wamba and its adjoining areas in north-central Nigeria. *Earth Sciences Research Journal* 16 (1): 25–33.

Arjmandzadeh R., Rashvanlou V. S., Dabiri R., Almasi A. (2017) Satellite thermal surveys to detecting hidden active faults and fault termination, Case study of Quchan fault, NE Iran. *Iranian Journal of Earth Sciences* 9 (1): 39–47.

Bakar Y. A., San Lim H., Abir I. A. (2023) Radiogenic heat production estimation towards sustainable energy drive in northeastern Nigeria. *Heliyon* 9 (6) DOI: https://doi.org/10.1016/j.heliyon.2023.e16310.

Bako A. S. J. (2010) Geothermal energy potential in the part of middle benue trough located in Nasarawa state. *A thesis submitted to the postgraduate school, Ahmadu Bello University, Zaria, Nigeria*

Bhattacharyya B. K., Leu L. K. (1977) Spectral analysis of gravity and magnetic anomalies due to rectangular prismatic bodies. *Geophysics* 42 (1): 41–50. DOI: https://doi.org/10.1190/1.1440712.

——— (1975) Spectral analysis of gravity and magnetic anomalies due to two-dimensional structures. *Geophysics* 40 (6): 993–1013. DOI: https://doi.org/10.1190/1.1440593.

Birch F. (1954) Heat from radioactivity. *Nuclear geology* 148:174.

Blakely R. J. (1996) Potential theory in gravity and magnetic applications. *Cambridge university press*

Cull J. P., Conley D. (1983) Geothermal gradients and heat flow in Australian sedimentary basin. *Journal of Austral Geology and Geophys* 8:332–337.

Debeglia N., Corpel J. (1997) Automatic 3-D interpretation of potential field data using analytic signal derivatives. *Geophysics* 62 (1): 87–96. DOI: https://doi.org/10.1190/1.1444149.

Dimgba B. C., Obiora D. N., Abangwu J. U., Ugbor D. O. (2020) Study of Curie point depth and heat flow from spectral analysis of aeromagnetic data for geothermal potential of Gubio, Chad Basin, Nigeria. *SN Applied Sciences* 2:1–9. DOI: https://doi.org/10.1007/s42452-020-3146-9.

Dopamu K. O., Akoshile C. O., Nwankwo L. I. (2021) Regional estimation of geothermal resources of the entire Benue Trough, Nigeria using high-resolution aeromagnetic data. *Geomechanics and Geophysics for Geo-Energy and Geo-Resources* 7:1–17. DOI: https://doi.org/10.1007/s40948-021-00276-z.

Ekwok S. E., Akpan A. E., Ebong E. D., Eze O. E. (2021) Assessment of depth to magnetic sources using high resolution aeromagnetic data of some parts of the Lower Benue Trough and adjoining areas, Southeast Nigeria. *Advances in Space Research* 67 (7): 2104–2119. DOI: https://doi.org/10.1016/j.asr.2021.01.007.

Eletta B. E., Udensi E. E. (2012) Investigation of the Curie point isotherm from the magnetic fields of eastern sector of central Nigeria. *Geosciences* 2 (4): 101–106. DOI: https://doi.org/10.5923/j.geo.20120204.05.

Haack U. (1982) Radioactivity of rocks. *Landolt-Börnstein Numerical Data and Functional Relationships in Science and Technology. New Series, Group V. Geophysics and Space Research, vol. 1, Physical properties of rocks, subvolume b., Springer-Verlag Berlin, Heidelberg,* 433–481.

Jessop A. M. (1976) Geothermal energy from sedimentary basins. *United State Department of Energy Office of Scientific and Technical Information,* no. NP. 22308. EDB-77-131177

Korenaga J. (2011) Clairvoyant geoneutrinos. *Nature Geoscience* 4 (9): 581–582. DOI: https://doi.org/10.1038/ngeo1240.

Kuforijimi O., Christopher A. (2017) Correlation and mapping of geothermal and radioactive heat production from the Anambra Basin, Nigeria. *African Journal of Environmental Science and Technology* 11 (10): 517–531. DOI: https://doi.org/10.5897/AJEST2017.2382.

Lay T., Hernlund J., Buffett B. A. (2008) Core–mantle boundary heat flow. *Nature Geoscience* 1 (1): 25–32. DOI: https://doi.org/10.1038/ngeo.2007.44.

McCay A. T., Harley T. L., Younger P. L., Sanderson D. C., Cresswell A. J. (2014) Gamma-ray spectrometry in geothermal exploration: State of the art techniques. *Energies* 7 (8): 4757–4780. DOI: https://doi.org/10.3390/en7084757.

Megwara J. U., Udensi E. E., Olasehinde P. I., Daniyan M. A., Lawal K. M. (2013) Geothermal and radioactive heat studies of parts of southern Bida basin, Nigeria and the surrounding basement rocks. *International Journal of Basic and Applied Science* 2 (1): 125–139. DOI: https://doi.org/10.14419/ijbas.v2i1.624.

Melouah O., Ebong E. D., Abdelrahman K., Eldosouky A. M. (2023) Lithospheric structural dynamics and geothermal modeling of the Western Arabian Shield. *Scientific Reports* 13 (1): 11764. DOI: https://doi.org/10.1038/s41598-023-38321-4.

Melouah O., Steinmetz R. L. L., Ebong E. D. (2021) Deep crustal architecture of the eastern limit of the West African Craton: Ougarta Range and Western Algerian Sahara. *Journal of African Earth Sciences* 183:104321. DOI: https://doi.org/10.1016/J.JAFREARSCI.2021.104321.

Nazari M., Arian M. A., Solgi A., Zareisahamieh R., Yazdi A. (2023) Geochemistry and tectonomagmatic environment of Eocene volcanic rocks in the Southeastern region of Abhar, NW Iran. *Iranian Journal of Earth Sciences* 15 (4): 228–247. DOI: https://doi.org/10.30495/ijes.2023.1956689.1746.

Ngene T., Mukhopadhyay M., Ampana S. (2022) Reconnaissance investigation of geothermal resources in parts of the Middle Benue Trough, Nigeria using remote sensing and geophysical methods. *Energy Geoscience* 3 (4): 360–371. DOI: https://doi.org/10.1016/j.engeos.2022.06.002.

NGSA (2009) Geological map of Nigeria *Nigeria Geological Survey Agency,* https://ngsa.gov.ng/geological-maps

Nwajide C. S. (1990) Cretaceous sedimentation and paleogeography of the central Benue Trough. *The Benue Tough structure and Evolution. International Monograph Series, Braunschweig,* 19–38.

Obaje N. G. (2009) Geology and mineral resources of Nigeria. *Springer* 120:221. DOI: https://doi.org/10.1007/978-3-540-92685-6.

Offodile M. E. (1976) The geology of the Middle Benue, Nigeria. *Palaentological Institute, University Uppsala, Special Publication* 4:1–166.

Okubo Y., Graf R. J., Hansen R. O., Ogawa K., Tsu H. (1985) Curie point depths of the island of Kyushu and surrounding areas, Japan. *Geophysics* 50 (3): 481–494. DOI: https://doi.org/10.1190/1.1441926.

Paterson N. R., Reeves C. V. (1985) Applications of gravity and magnetic surveys; the state-of-the-art in 1985. *Geophysics* 50 (12): 2558–2594. DOI: https://doi.org/10.1190/1.1441884.

Ramadass G., SubhashBabu A., Udaya Laxmi G. (2015) Structural analysis of airborne radiometric data for identification of Kimberlites in parts of eastern Dharwar Craton. *International Journal of Science and Research* 4 (4): 2375–2380.

Ravat D., Pignatelli A., Nicolosi I., Chiappini M. (2007) A study of spectral methods of estimating the depth to the bottom of magnetic sources from near-surface magnetic anomaly data. *Geophysical Journal International* 169:421–434. DOI: https://doi.org/10.1111/j.1365-246X.2007.03305.x.

Roest W. R., Verhoef J., Pilkington M. (1992) Magnetic interpretation using the 3-D analytic signal. *Geophysics* 57 (1): 116–125. DOI: https://doi.org/10.1190/1.1443174.

Rybach L. (1976) Radioactive heat production: A physical property determined by the chemistry of rocks. *The Physics and Chemistry of Minerals and Rocks, Wiley-Interscience,* 309–318.

Saadat S., Ghoorchi M., Dabiri R. (2023) Extracting clay minerals with emphasis on Bentonite in Eastern Iran, using Landsat 8 and ASTER images. *Iranian Journal of Earth Sciences* 15 (3): 188–194. DOI: https://doi.org/10.30495/ijes.2023.1973739.1815.

Salako K. A., Adetona A. A., Rafiu A. A., Alahassan U. D., Aliyu A., Adewumi T. (2020) Assessment of geothermal potential of parts of Middle Benue Trough, North-East Nigeria. *Journal of the Earth and Space Physics* 45 (4): 27–42. DOI: https://doi.org/10.22059/jesphys.2019.260257.1007017.

Sanusi S. O., Amigun J. O. (2020) Structural and hydrothermal alteration mapping related to orogenic gold mineralization in part of Kushaka schist belt, North-central Nigeria, using airborne magnetic and gamma-ray spectrometry data. *SN Applied Sciences* 2:1–26. DOI: https://doi.org/10.1007/s42452-020-03435-1.

Schmeling H., Marquart G., Weinberg R., Wallner H. (2019) Modelling melting and melt segregation by two-phase flow: new insights into the dynamics of magmatic systems in the continental crust. *Geophysical Journal International* 217 (1): 422–450. DOI: https://doi.org/10.1093/gji/ggz029.

Spector A., Grant F. S. (1970) Statistical models for interpreting aeromagnetic data. *Geophysics* 35 (2): 293–302. DOI: https://doi.org/10.1190/1.1440092.

Stacey F. D. (1977) A thermal model of the Earth. *Physics of the Earth and Planetary Interiors* 15 (4): 341–348. DOI: https://doi.org/10.1016/0031-9201(77)90096-6.

Tanaka A., Okubo Y., Matsubayashi O. (1999) Curie point depth based on spectrum analysis of the magnetic anomaly data in East and Southeast Asia. *Tectonophysics* 306 (3-4): 461–470. DOI: https://doi.org/10.1016/S0040-1951(99)00072-4.

Trifonova P., Zhelev Z., Petrova T., Bojadgieva K. (2009) Curie point depths of Bulgarian territory inferred from geomagnetic observations and its correlation with regional thermal structure and seismicity. *Tectonophysics* 473 (3-4): 362–374. DOI: https://doi.org/10.1016/j.tecto.2009.03.014.

Čermák V., Rybach L. (1982) Thermal conductivity and specific heat of minerals and rocks. *Landolt-Börnstein: Numerical Data and Functional Relationships in Science and Technology, New Series, Group V (Geophysics and Space Research), Volume Ia, (Physical Properties of Rocks), Springer Berlin-Heidelberg,* 305–343.

Šrámek O., McDonough W. F., Kite E. S., Lekić V., Dye S. T., Zhong S. (2013) Geophysical and geochemical constraints on geoneutrino fluxes from Earth's mantle. *Earth and Planetary Science Letters* 361:356–366. DOI: https://doi.org/10.1016/j.epsl.2012.11.001.